Electronic Supplementary Material (ESI) for Materials Horizons.

Supporting Information

Engineering crack tortuosity in printed polymer-polymer composites through ordered pores

Luke F. Gockowski[a,†], Neil D. Dolinski[b,†], Roberto Chavez[c], Noy Cohen[d], Fabian Eisenreich[e], Stefan Hecht[e], Robert M. McMeeking[a,b,f,g], Craig J. Hawker[b,c,*], and Megan T. Valentine[a,*]

[a] *Department of Mechanical Engineering, University of California Santa Barbara, Santa Barbara, CA 93106*
[b] *Department of Materials, University of California Santa Barbara, Santa Barbara, CA 93106*
[c] *Department of Chemistry and Biochemistry, University of California Santa Barbara, Santa Barbara, CA 93106*
[d] *Department of Materials Science and Engineering, Technion – Israel Institute of Technology, Haifa 3200003, Israel*
[e] *Department of Chemistry and IRIS Adlershof, Humboldt-Universität zu Berlin, 12489 Berlin, Germany*
[f] *School of Engineering, University of Aberdeen, King's College, Aberdeen AB24 3UE, UK*
[g] *INM - Leibniz Institute for New Materials, 66123 Saarbrücken, Germany*
† These authors contributed equally to this work

Table of Contents

1. Experimental Details

A. Materials.

All chemicals were used as received unless otherwise noted. Aluminum oxide activated (basic, Brockmann I), methyl acrylate (MA, 99%, contains ≤100 ppm monomethyl ether hydroquinone as inhibitor), tetra(ethylene glycol) diacrylate (TEGDA, technical grade, contains 150-200 ppm MEHQ as inhibitor, 100-150 ppm HQ as inhibitor), 3,4-epoxycyclohexylmethyl 3,4-epoxycyclohexanecarboxylate (ECC), acryloyl chloride (≥97%, contains ~400 ppm phenothiazine as stabilizer), 2-methylthianaphthene (97%), and triethylamine (TEA, ≥99.5%) were purchased from Sigma Aldrich. Inhibitors were removed from MA and TEGDA by a plug of basic alumina. L-camphorquinone (CQ, 99%), benzothiophene (97%), and n-butyllithium (2.3 M solution in cyclohexane) were purchased from ACROS organics™. (3-ethyloxetan-3-yl)methanol (OXA. 98%) was purchased from Arc Pharm Inc. and used as received. Ethyl 4-(dimethylamino)benzoate (EDMAB, 99%) was purchased from Alfa Aesar. [4-[Octyloxy]phenyl]phenyliodonium hexafluoroantimonate (HNu_{254}), 2-(butyryloxy)-N,N,N-trimethylethan-1-aminium butyltriphenylborate (Borate), and 6-hydroxy-2,4,5,7-tetraiodo-3H-xanthen-3-one (HNu_{535}) were purchased from Spectra group limited. Octafluorocyclopentene (>98%) was purchased from TCI. XHT-500 fluorinated oil was purchased from Grainger.

All printed materials were produced by exposure to light produced by an Epson 5040UB 3 LCD projector focused through a Zeiss Bronica Zenzanon-S lens (105 mm, f/3.5).

B. Instrumentation.

Displacement-controlled uniaxial tensile testing was performed on a vertical TwinRail positioning table (Lintech, CA) with a Lebow Load Cell (Model 3108–10, 10-lb capacity, Eaton Corp., MI) fitted with a machined sample holder.

Optical microscopy was performed on a Keyence VHX-5000 Microscope at 10x-20x magnification.

A Canon Rebel SL2 (100 mm, f/2.8 Macro USM fixed lens, 1x magnification, 30 frames per second) was used to image the deformation of each sample during mechanical testing (see supplemental movies).

C. Synthesis.

Synthesis of (3-ethyloxetan-3-yl)methyl acrylate (OXA-A)

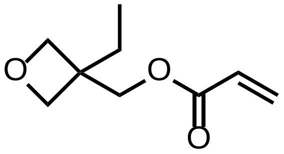

The synthesis of OXA-A was conducted according to previously reported protocols.[1]

Synthesis of 1,2-bis(3-methyl-1-benzothiophen-2-yl)perfluorocyclopentene (DAE$_{470}$) open and closed isomers

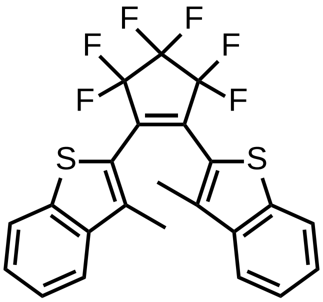

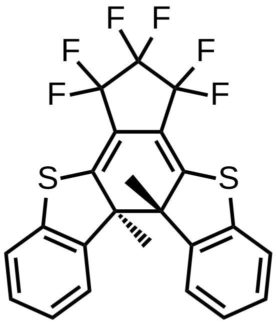

The synthesis of both the open (left) and closed (right) isomers of DAE470 were conducted according to previously reported protocols.[1]

Synthesis of 1,2-bis(2-methyl-1-benzothiophen-3-yl)perfluorocyclopentene (DAE$_{530}$) open and closed isomers

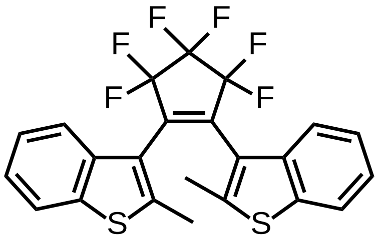

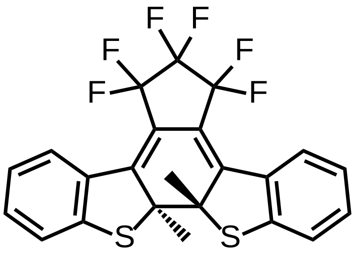

The synthesis of both the open (left) and closed (right) isomers of DAE$_{470}$ were conducted according to previously reported protocols.[1,2]

D. Resin formulation.

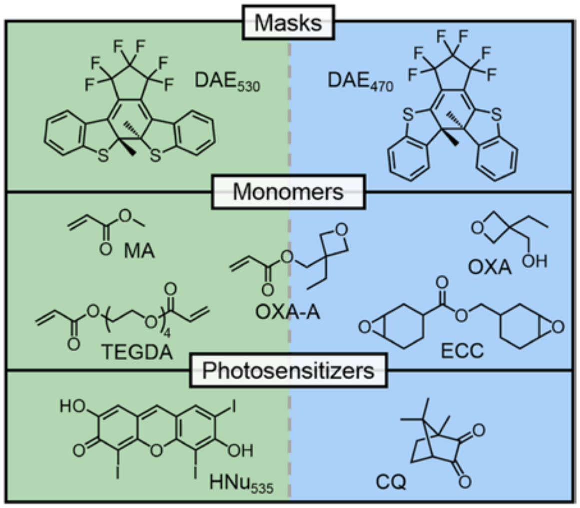

Figure S1. Chemical structures of select components in SMaLL resins used in this work**.**

Table S1. Weight percentages and function of chemical species in SMaLL resins used in this work

Species	Function	Loading (wt%)	
MA	Radical monomer	50	**Majority components**
OXA-A	Network compatibilizer	5	
OXA	Cationic initiator / monomer	10	
ECC	Cationic crosslinker	35	
TEGDA	Radical crosslinker	0.5	**wt% relative to majority components**
Borate	Radical accelerator	0.05	
EDMAB	Cationic accelerator	0.2	
HNu$_{535}$	Photosensitizer	0.01	
CQ	Photosensitizer	0.2	
HNu$_{254}$	Coinitiator	0.45	
DAE$_{530}$	Solution mask	8 mM	**mM instead of wt%**
DAE$_{470}$	Solution mask	10 mM	

E. Sample Preparation.

The printing of the reported samples follows previous literature conditions[1], summarized here. A surface treated (perfluoroalkyl) glass build plate was adhered to the bottom of a custom build chamber using a fluorinated oil (XHT-500). The septa-sealed chamber was then purged with argon and ~3 mL of degassed resin was transferred into the chamber. The build chamber was placed in custom brackets over a projector (Epson 5040UB 3 LCD) equipped with a photography lens (Zeiss Bronica Zenzanon-S lens, 105 mm, f/3.5). The resin was then exposed to digital images. Blue segments of the images were exposed for 6.5 minutes (if applicable) followed by exposure all non-black regions (i.e., pores) in green for 2 minutes to ensure strong connectivity between segments. After exposure, residual resin was retrieved via syringe and recycled for future prints.

The printed part was then removed from the build plate with a razor blade and introduced into a dialysis chamber to remove any unreacted monomers from the sample. Dialysis was carried out with mixtures of acetone:isopropanol (vol:vol 3:1, 1:1, 1:3) prior to drying overnight in air followed by storage in a vacuum chamber. Dried samples were adhered to laser-cut fiberglass tabs using a generic cyanoacrylate-based adhesive. This method was used to avoid applying unwanted stresses to the samples orthogonal to the loading axis.

2. Sample Design.

A. Notch-free sample templates.

All templates for solution mask liquid lithography (SMaLL) printing were designed in Microsoft PowerPoint and then projected onto resin baths using the above methods. Fig. S2 illustrates sample templates used for printing square-packed, hexagonally-packed, and pore-free samples and the resulting specimens. To simplify the comparison between samples, the area fraction of pores was held constant (51 ± 3%), as was the center-to-center distance between pores as measured along the horizontal and vertical axes of the structure. The hexagonal packing was achieved by simply shifting the pore position of every other horizontal row (defined along the long axes of the structure) by ½ of the center-to-center distance between pores and adding one additional pore to maintain left-right symmetry. This results in non-equal-sided hexagons that are slightly elongated along the vertical direction. A red outline of these shapes is illustrated in Fig. S2a.

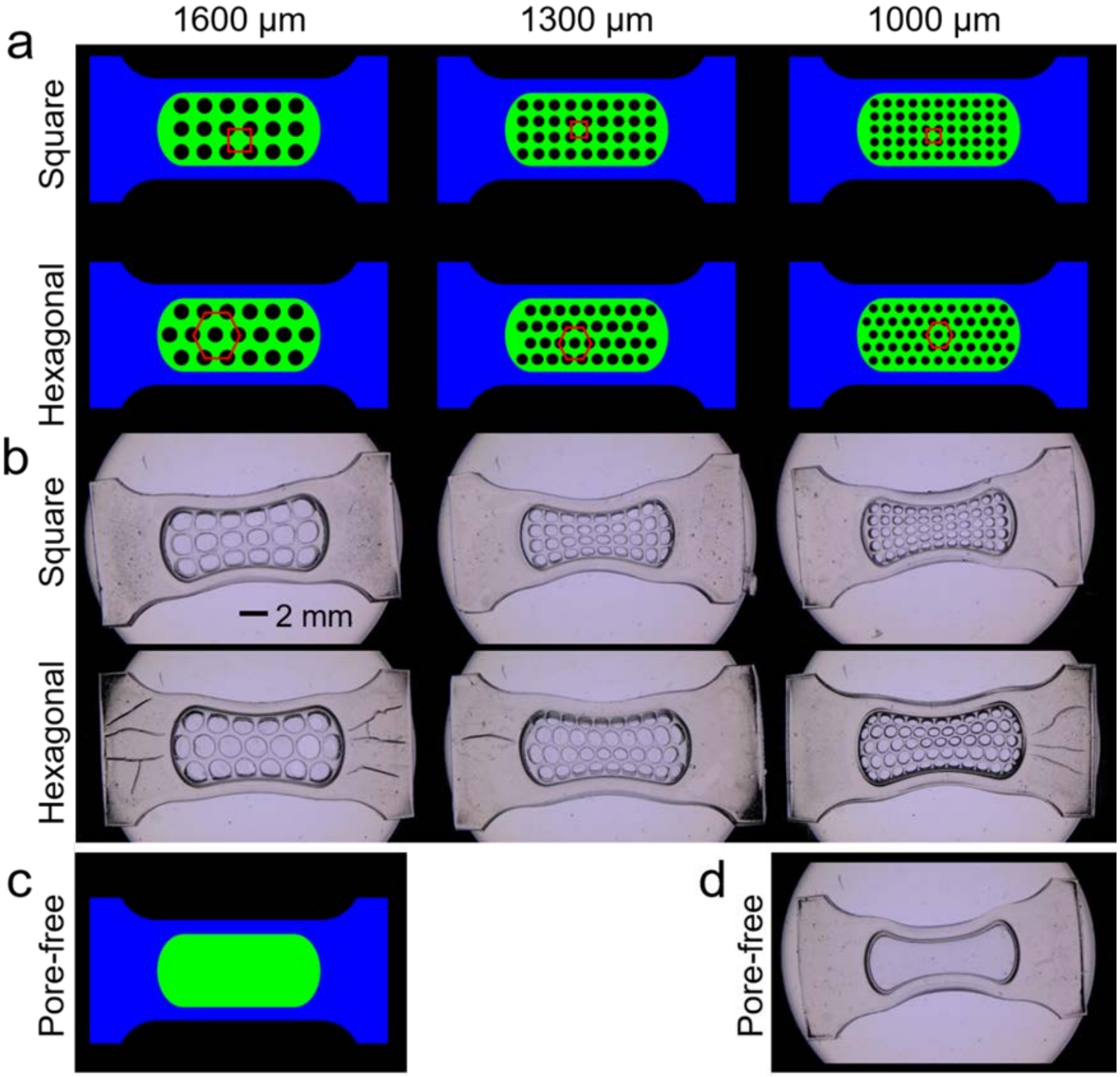

Fig. S2. a) SMaLL printing templates used for hex- and square-packed samples for all pore sizes. b) Optical microscope images of printed pore-containing specimens after dialysis and drying. c) SMaLL printing templates used for pore-free samples. d) Optical microscope image of a pore-free specimen after dialysis and drying.

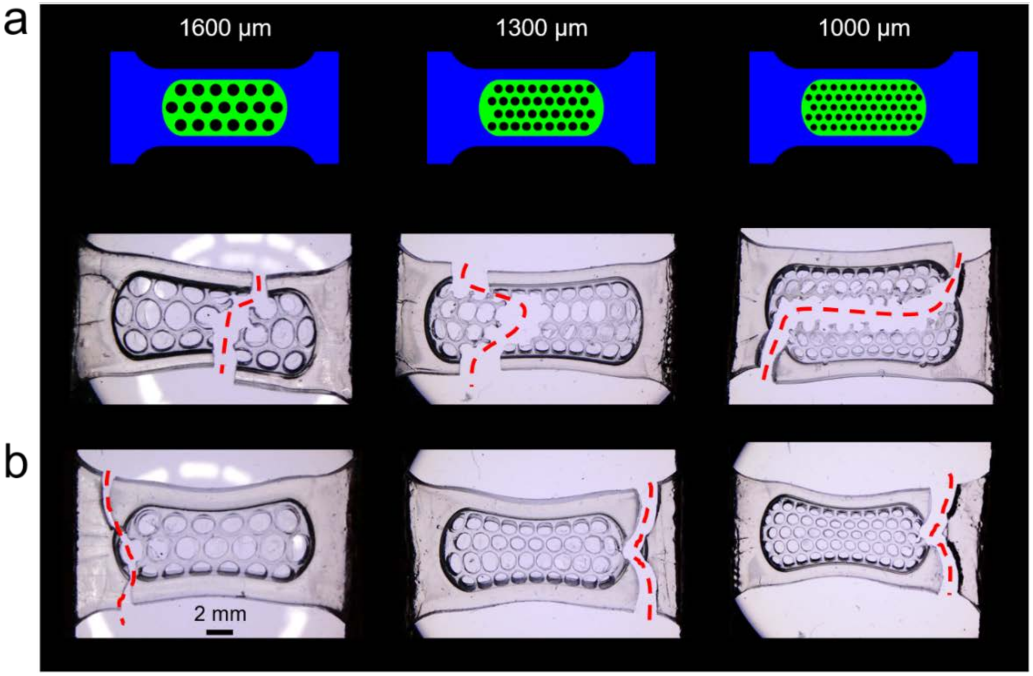

Fig. S3. a) Examples of crack paths (demarcated here forth by red dashed lines) for notch-free hexagonally-packed samples demonstrating increasing crack tortuosity as a function of reducing pore size, however these failures can largely be attributed to well-positioned stochastic failure in the stiff blue exterior. b) Examples of poor crack deflection in notch-free hexagonally-packed samples, demonstrating the need for repeatable crack initiation points (notched, below).

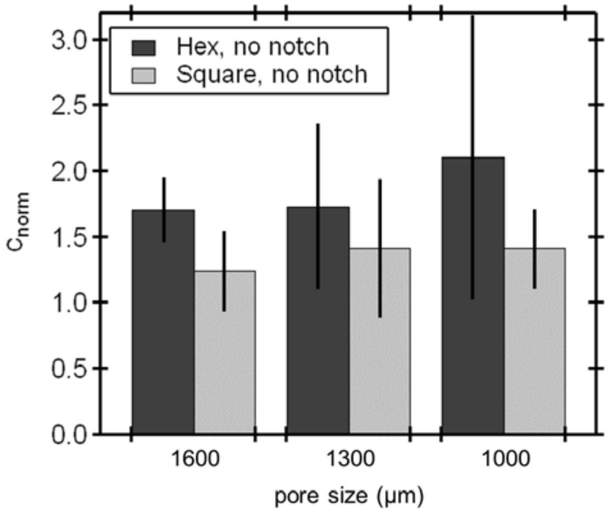

Fig. S4. Impact of pore size and packing of voids on crack tortuosity in hexagonally- and square-packed samples without notches. Without controlling the location of crack initiation (via notches), the crack lengths measured vary widely for all sample geometries, highlighting the importance of using notched samples.

B. Notched sample templates.

All templates for solution mask liquid lithography (SMaLL) printing were designed in Microsoft PowerPoint and then projected onto resin baths using the above methods. Fig. S5a illustrates sample templates used for notched square-packed and hexagonally-packed samples.

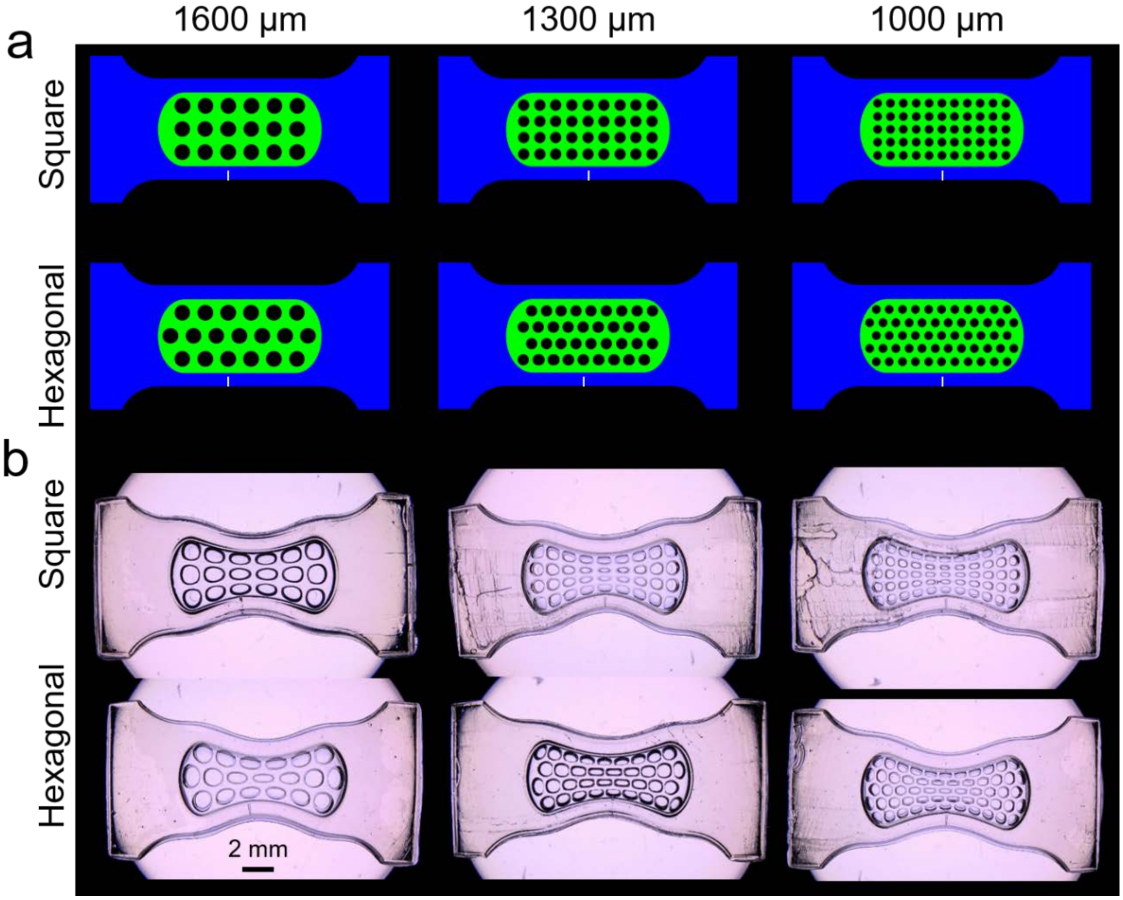

Fig. S5. a) SMaLL printing templates and b) resulting samples used for the notched square- and hex- packed cases.

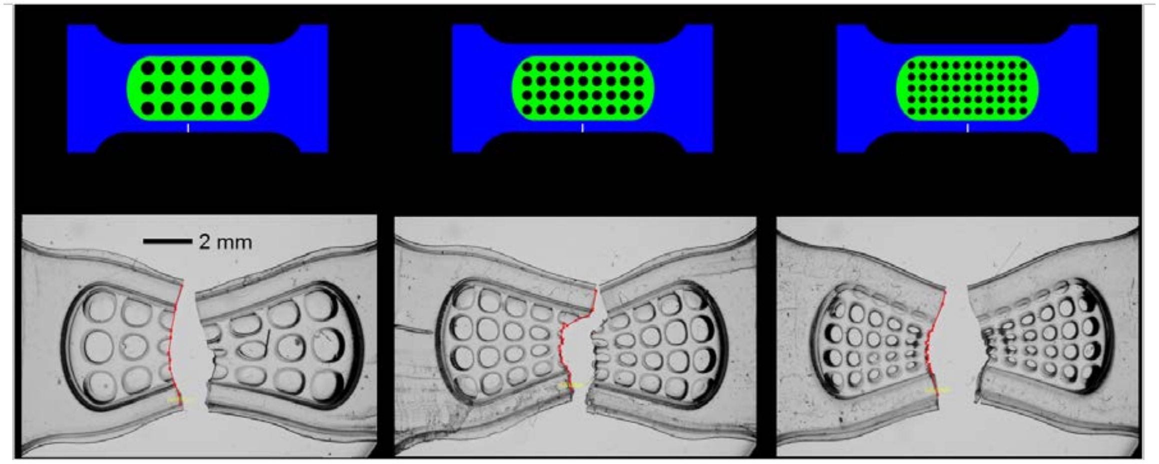

Fig S6. Representative failures of notched samples with square-packed pores (outline crack path with red line).

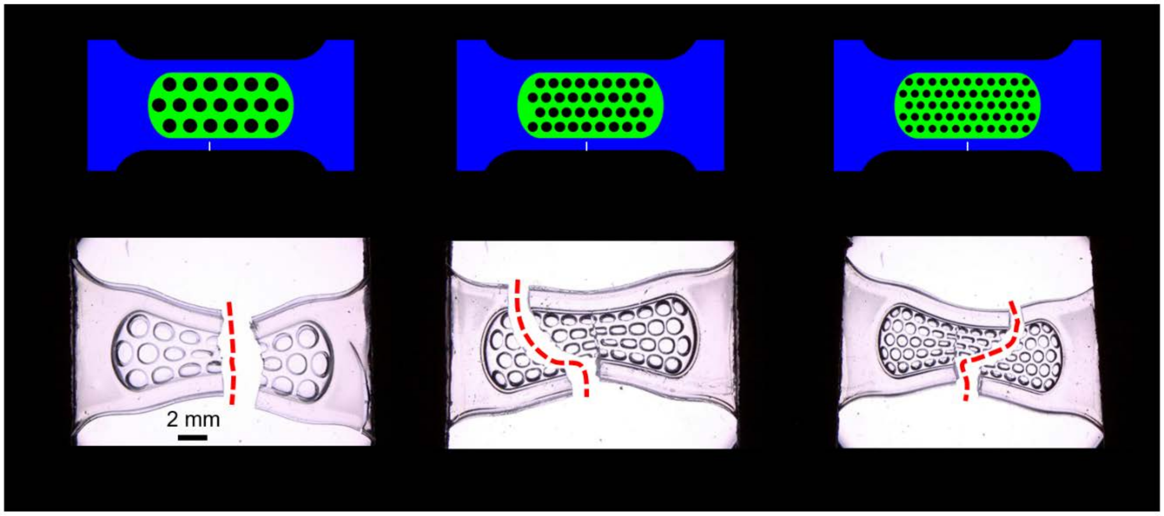

Fig S7. Representative failures of notched samples with hexagonally-packed pores (outline crack path with dashed red line).

3. Characterization.

A. Mechanical testing and imaging.

Using the aforementioned tensile testing apparatus, all samples were tested at a fixed strain rate of 100% min^{-1}. Forces and displacements recorded during tensile testing were then converted to engineering stresses and engineering strains using cross-sectional area (including pores in the core area) and length measurements performed using the Keyence VHX-5000's built-in software. Post mechanical testing, Keyence's built-in software was used to calculate crack length.

A Canon Rebel SL2 was used to image the deformation of each sample during mechanical testing (see supplemental movies). Fig. S8b offers a screenshot from a recording of mechanical testing.

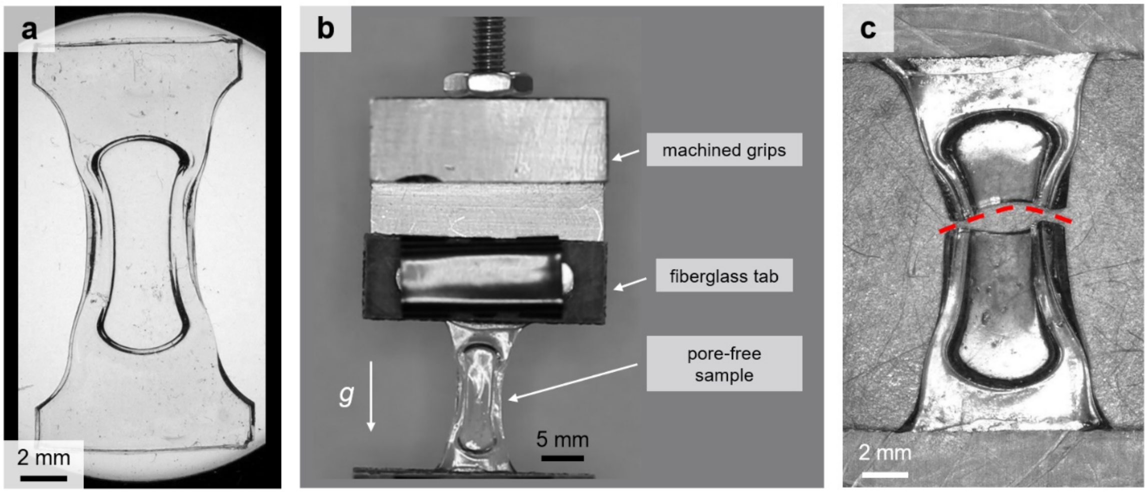

Fig. S8. Imaging before, during, and after mechanical testing. a) A pore-free composite imaged on the Keyence VHX-5000. b) A screenshot from a video recording of a tensile test, illustrating the different components of the tensile testing setup. c) An image of the fractured composite obtained using the Keyence VHX-5000.

B. Mechanical properties of notched samples.

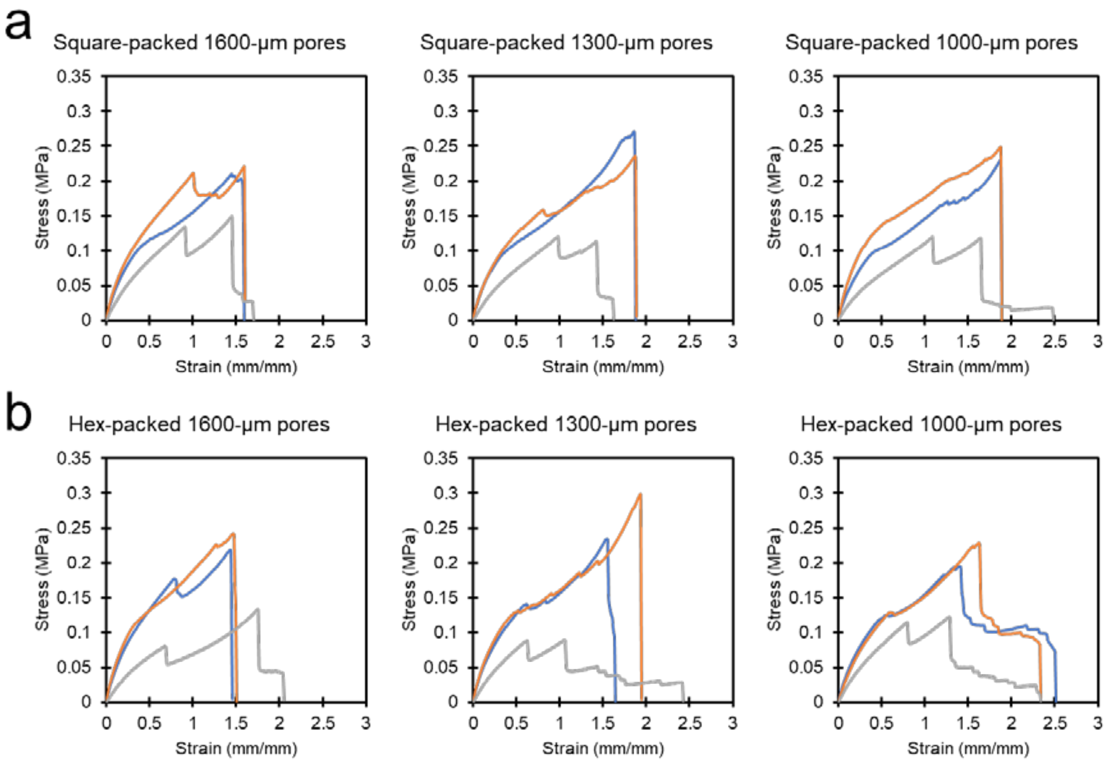

Fig. S9. a) Nominal stress-strain curves for square-packed samples, demonstrating limited increases in ultimate strain as a function of reduced pore size due to near-linear crack paths. b) Stress-strain curves for hexagonally-packed samples, showing large increases in ultimate strain with similar tensile response.

4. Simulations.

A. Material fits.

The stress-strain response of constituent radical (green) and dual-cured radical/cationic (blue) materials were fitted to hyper-elastic models. The dual-cured material follows a Yeoh model (Fig. S10) while the radical material follows the Mooney-Rivlin model (Fig. S11). Both materials were assumed to be incompressible. The strain energy density in the Yeoh model is defined as $W = c_1(I_1 - 3) + c_2(I_1 - 3)^2 + \mathrm{c}_3(I_1 - 3)^3$ where I_1 is the first invariant of the Cauchy-Green deformation tensor and c_n is the n^{th} constant. Using a fit to experimental results from a simple tensile test, it was found that $c_1 = 0.136\ MPa$, $c_2 = -3.2\ KPa$, and $c_3 = 2.7\ KPa$. The strain energy density in the Mooney-Rivlin model is defined as $W = c_1(I_1 - 3) + c_2(I_2 - 3)$, where I_2 is the second invariant Cauchy-Green deformation tensor and c_n is the n^{th} constant. Here, a fit to the stress-strain data obtained by tensile test of dog bone samples of uniform radical (green) material reveals that $c_1 = 0.01\ \mathrm{MPa}$ and $c_2 = 0.083\ \mathrm{MPa}$.

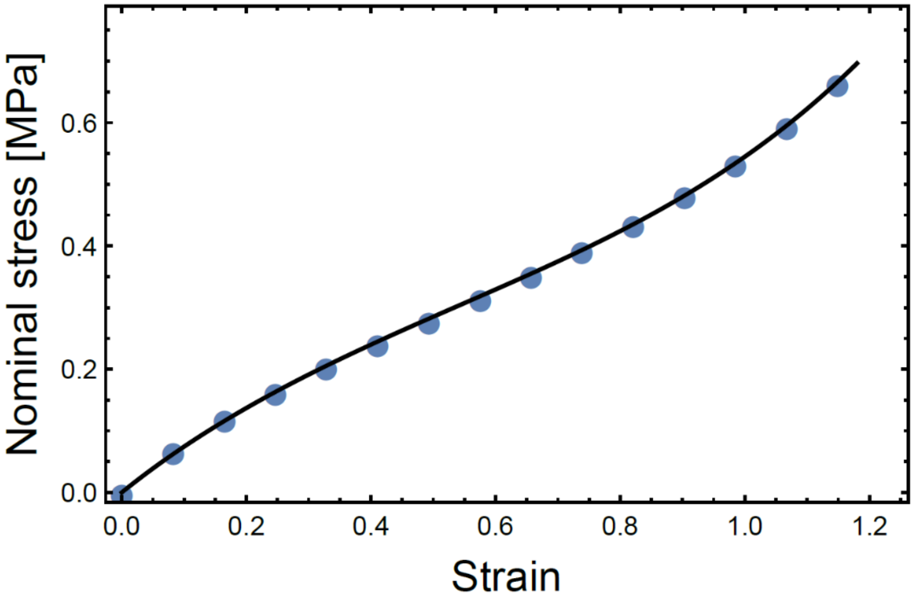

Fig. S10. Fit to the (nominal) stress-strain data obtained for a uniform dual-cured radical/cationic material (obtained by curing with blue light only) subjected to uniaxial stretch, using a Yeoh hyper-elastic material model.

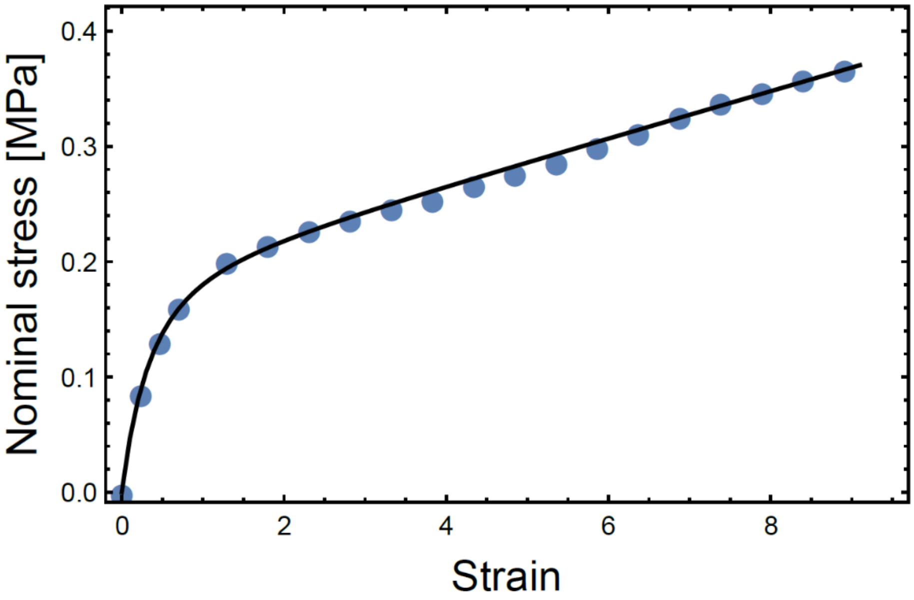

Fig. S11. Fit to the (nominal) stress-strain data obtained for a uniform radical cured constituent material (obtained by curing with green light only) subjected to uniaxial stretch, using a Mooney Rivlin hyper-elastic material model.

B. Finite Element Analysis.

A two-dimensional analysis of the square- and hexagonally-packed porous samples was performed in COMSOL under plane-stress conditions. The samples were subjected to uniaxial engineering strains of 100%. The results below are the maximum tensile principal stresses obtained for samples with hexagonally-packed 1600-µm (Fig. S12) and 1000-µm (Fig. S13) pores, as well as simulated samples with square-packed 1600-µm (Fig. S14) and 1000-µm (Fig. S15) pores.

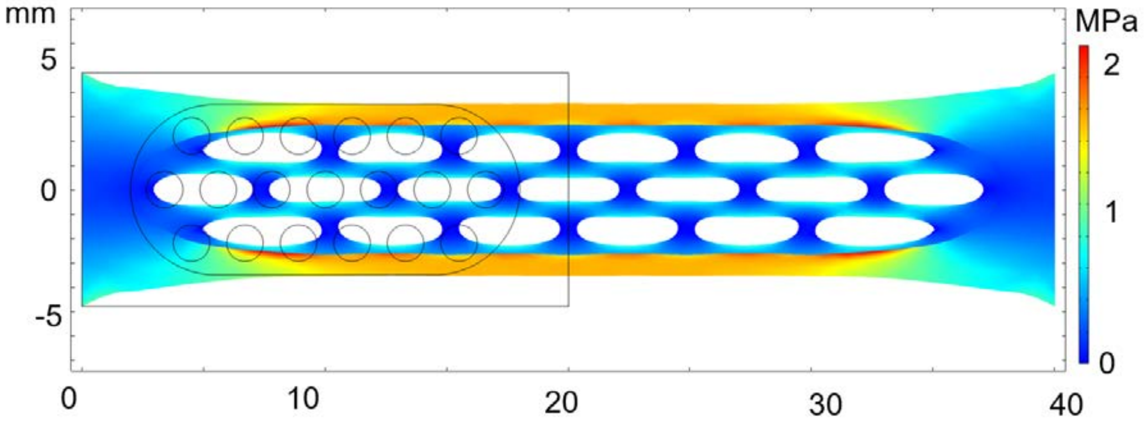

Fig S12. Maximum principal stresses of simulated sample with hexagonally-packed, 1600-µm pores, here shown at 100% strain. The thin black outline depicts the sample at 0% strain.

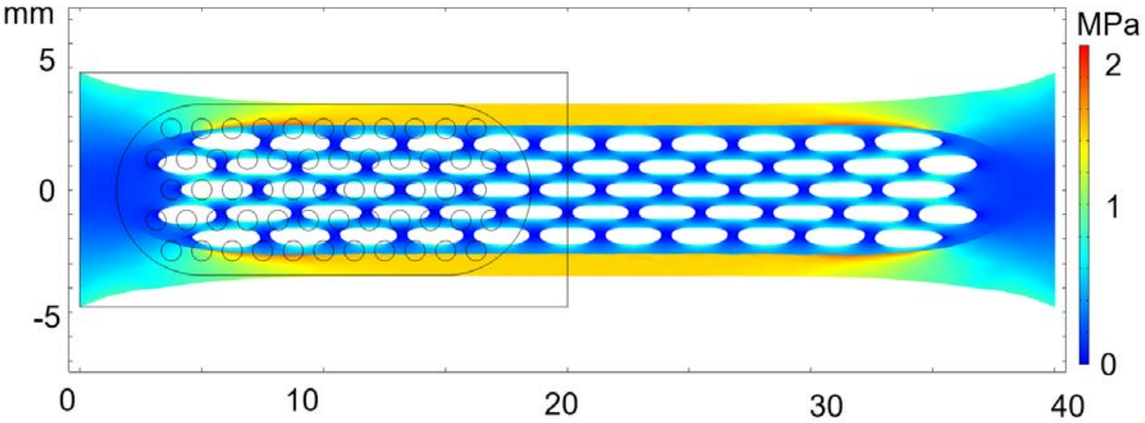

Fig S13. Maximum principal stresses of simulated sample with hexagonally-packed, 1000-µm pores at 100% strain. The thin black outline depicts the sample at 0% strain.

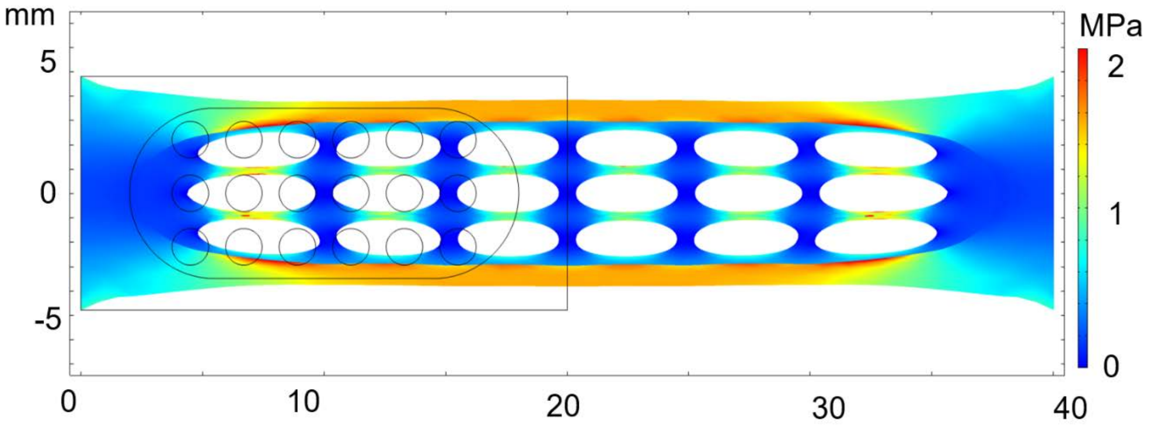

Fig S14. Maximum principal stresses of a simulated sample with square-packed, 1600-µm pores, at 100% strain. The thin black outline depicts the sample at 0% strain.

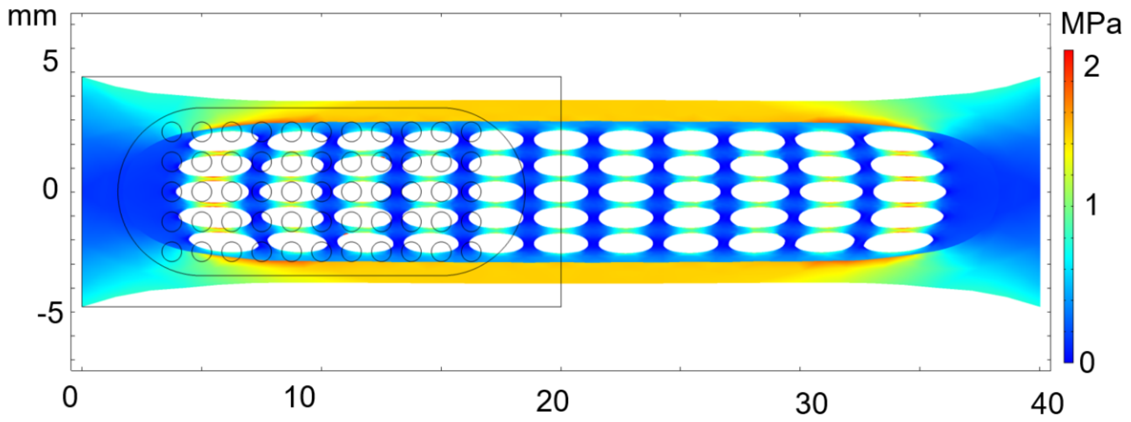

Fig S15. Maximum principal stresses of a simulated sample with square-packed, 1000-µm pores at 100% strain. The thin black outline depicts the sample at 0% strain.

C. Tortuosity Model

We consider samples with a limited number of pores as shown in their undeformed configurations in Figs. S16 & S17. The stiff shell of the sample is represented by the material shaded grey, and the core material has a hexagonal arrangement of pores. The pore volume fraction is assumed to be the same for both samples, so that the ratio *D*/*S* is fixed. For simplicity, the distance from the pore centers nearest the stiff shell to the free surface of the stiff shell is set equal to *S*. As a consequence, the width of the sample in Fig. S16 is $(2+\sqrt{3}/2)S$ and that of the sample in Fig. S17 is $(2+\sqrt{3})S$.

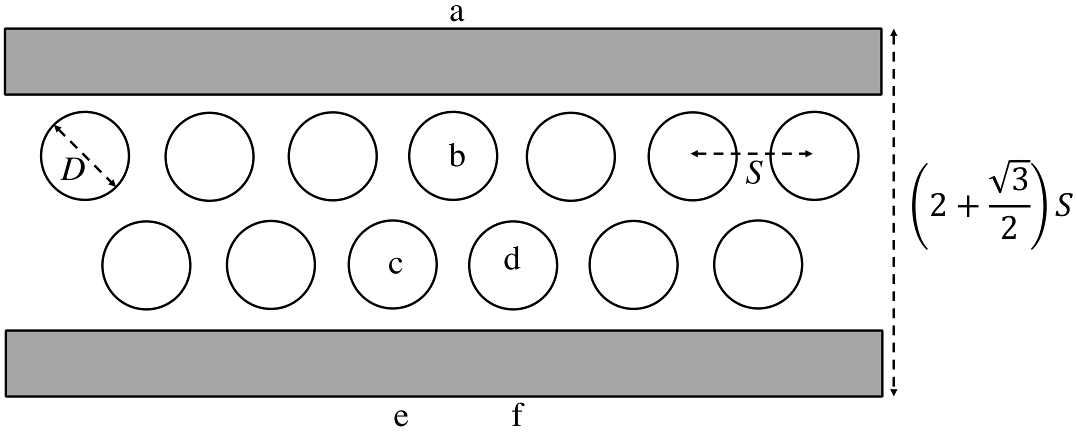

Fig. S16. A sample with 2 columns of pores in a hexagonal arrangement.

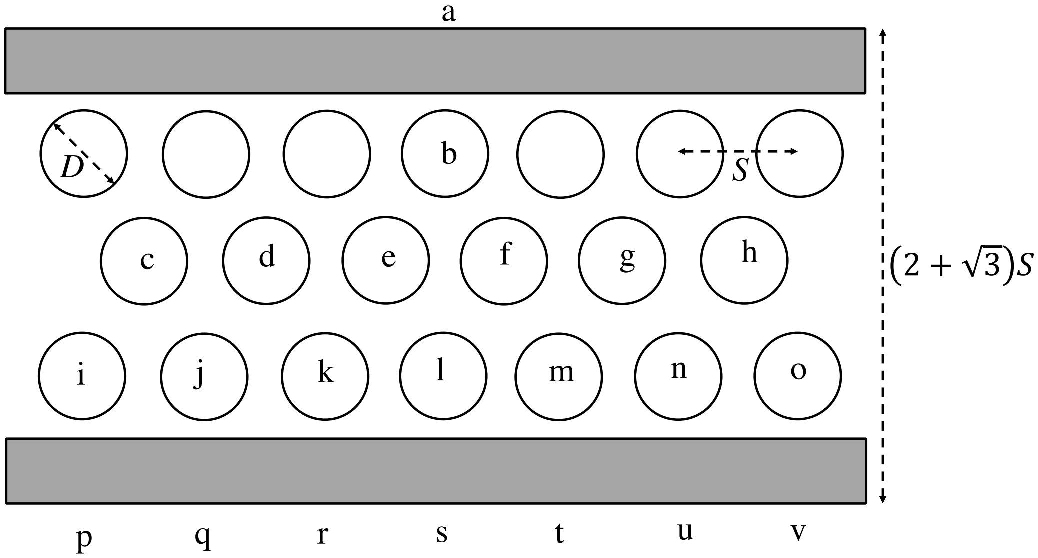

Fig. S17. A sample with 3 columns of pores in a hexagonal arrangement.

The samples are stretched in the horizontal direction to an extent comparable with the strain levels depicted in Figs. 6b, S12 & S13 or higher, whereupon ligaments begin to break, starting with ab in both cases. The finite element result in Fig. 6b shows that the highest stress occurs in the ligament between nearest neighbor pores in adjacent columns. If the strength of the polymer in the core is deterministic, then the ligaments that break next in the sample in Fig. S16 upon further stretching will be either bc or bd. We assume small variations in the width of the ligaments will bias the system to break either bc or bd but not both. We further assume that once one of those ligaments has ruptured, the stiff ligament between the crack tip and the sample free surface will break spontaneously, and sample fracture will have been completed. That is, if ligament bc has ruptured, ligament ce follows, and if ligament bd has ruptured, ligament df then does so. The path length of both of these possible rupture contours is 3*S*, and therefore, the degree of their tortuosity is

$$c_{norm} = \frac{3S}{\left(2+\frac{\sqrt{3}}{2}\right)S} = 1.05 \qquad \text{(S1)}$$

We now consider the sample depicted in Fig. S17. After the ligament ab breaks, the next one to fail will either be be or bf. If the crack tip is at e, the next increment of the fracture path will be either ek or el. If the tip is at f, then fl or fm will be the next ligament to rupture. If the crack tip reaches k, the ligament kr will spontaneously break, if it is at l, it will be ls that breaks and from m it will be mt that ruptures. Therefore, there are 4 possible crack paths depending on the variations in the ligament widths. However, all 4 possible paths have a contour length equal to 4*S* and the degree of tortuosity for all 4 is

$$c_{norm} = \frac{4S}{(2+\sqrt{3})S} = 1.07 \qquad \text{(S2)}$$

Thus, an increase in the number of pores, equivalent to the reduction in their size to achieve a given sample width, brings about a modest increase in the degree of tortuosity that does not appear to be consistent with the results in Fig. 5 for the hexagonal arrangement of pores. Even if asymmetry in the pattern of stresses develops in the sample depicted in Fig. S17 as a result of the deviated crack path, such asymmetry must develop within the hexagonal arrangement of pores. The preference for rupturing the most highly stressed ligament will still bring about a crack path having a degree of tortuosity equal to that in Eq. (S2). In addition, it is difficult to see why the deterministic process just described would bring about a significant increase in the strain to failure in the sample depicted in Fig. S17 compared to that for the sample in Fig. S16. Although further work is required to obtain definitive insights, a preliminary assessment suggests that the rupture process in both the sample in Fig. S16 and the sample in Fig. S17 will probably be an unstable one in both samples once 2 ligaments have rupture, a condition that we can expect to occur at a similar strain in both cases.

Now consider an alternative hypothesis in which rupture of ligaments is stochastic, perhaps due to spatial variations in the strength of the polymer, variations in the widths of ligaments, or the presence of small defects within the sample due to slight imperfections in manufacturing. We apply this hypothesis to all ligaments other than those between the stiff shell of material and the adjacent column of pores; we continue to assume that if the crack tip reaches such a pore, the ligament between it and the free surface of the stiff shell will spontaneously fracture. In addition, we introduce another 2 restrictive assumptions, namely that the deviation of the crack from its last increment of growth cannot exceed 60° and that a crack that has reached the central column of pores in the sample in Fig. S17 cannot return back to the column containing pore b. For simplicity, we allow the crack tip equal possibility of rupturing any of the ligaments between it and its nearest neighbor pores, given the restrictions stated above.

With these assumptions, the first 2 ligament ruptures in the stochastic case are unchanged from the quasi-deterministic model quantified above. That is, in both cases the 1st ligament rupture is still ab in both cases, followed by either bc or bd for the sample in Fig. S16 and by either be and bf for the sample in Fig. S17. Given the restrictions above, the only possible destinations for the crack in the sample in Fig. S16 are e and f, and the degree of tortuosity will therefore be given by the result in Eq. (S1). In contrast, the crack in the sample in Fig. S17 can exhibit a much wider range of possible crack paths. For example, rupture of bf can be followed by tearing of fg, or fm, or fl (but not fe). In addition, the crack that has reached f may proceed to pore g followed by pore h, thence to o and finally to v.

To estimate the degree of tortuosity of the crack path for the sample in Fig. S17, we compute a probability for each permitted crack path and calculate its degree of tortuosity. We then obtain the expected value of the degree of tortuosity by multiplying the degree of tortuosity for each crack path by its probability (set equal in this simple example) and sum over all permitted crack paths. The result of such a computation for the exact pore pattern in Fig. S17 is $\bar{c}_{norm} = 1.21$, and for a very long strip it rises to approximately 1.25. For the experimental sample in Fig. S5 with 1600 μm pores in a hexagonal arrangement, the same stochastic assumptions give an expected value for the degree of tortuosity of 1.18, approximately the same as the highest value observed experimentally for a notched specimen.

We thus deduce that stochastics play a role in the higher degrees of tortuosity observed experimentally for cracks in specimens having smaller pores and thus more columns of pores for a fixed specimen width. It is possible that small printing defects also play a more prominent role in specimens containing smaller feature sizes. In addition, the higher strains to failure observed for specimens having a higher degree of tortuosity can be rationalized as being possibly due to the higher strain and local stress required to rupture more of the stronger ligaments in a system having a probabilistic distribution of ligament strengths. Such insights are relevant to the analysis of natural porous materials, which typically contain disordered networks with polydisperse ligaments and pores.[3]

To some degree, the results in this section are speculative as they have been obtained without any significant application of mechanics, but rather by deductions based on geometry and probability leavened by a small dose of mechanics results. A more complete theoretical treatment of the mechanics of crack propagation will enable the production of a stronger foundation for the understanding of the phenomena involved.

5. Description of additional supplementary files.

Movie S1.
Fracture of a pore-free sample.

Movie S2.
Fracture of an un-notched hexagonally-packed, small pore (mean pore diameter = 1000 μm) sample.

Movie S3.
Fracture of a notched hexagonally-packed, small pore (mean pore diameter = 1000 μm) sample.

Movie S4.
Fracture of a notched square-packed, small pore (mean pore diameter = 1000 μm) sample.

Movie S5.
Fracture of an un-notched square-packed, small pore (mean pore diameter = 1000 μm) sample.

References

1 N. D. Dolinski, Z. A. Page, E. B. Callaway, F. Eisenreich, R. V. Garcia, R. Chavez, D. P. Bothman, S. Hecht, F. W. Zok and C. J. Hawker, *Adv. Mater.*, 2018, **1800364**, 1800364.

2 N. D. Dolinski, Z. A. Page, F. Eisenreich, J. Niu, S. Hecht, J. Read de Alaniz and C. J. Hawker, *ChemPhotoChem*, 2017, **1**, 125–131.

3 E. Filippidi, D.G. DeMartini, P. Malo de Molina, E.W. Danner, J. Kim, M.E. Helgeson, J.H. Waite and M.T. Valentine. *J. Royal Soc. Interf.* 2015, **12**(113) 20150827.